Journal of Power Sources 662 (2026) 238768

Contents lists available at ScienceDirect

Journal of Power Sources

journal homepage: www.elsevier.com/locate/jpowsour

Unleashing the potential in energy storage: The impact of redox electrolytes on specific energy in an asymmetric supercapacitor

Hellen Ngunya Mutua [a,b], Delvina Japhet Tarimo [a,*], Vusani Maphiri [a], Gift Rutavi [a], Julius Mwabora [b], Robinson Musembi [b], Ncholu Manyala [a,**]

[a] Department of Physics, SARChI in Nano-Materials for Energy Storage and Water Purification Applications, University of Pretoria, Pretoria, 0028, South Africa
[b] Department of Physics, University of Nairobi, P.O. Box 30197-00100, Nairobi, Kenya

HIGHLIGHTS

- Chronoamperometric electrodeposition was used for composite synthesis.
- A redox additive improved the aqueous electrolyte performance.
- Redox electrolyte influences charge storage in composite materials.
- Improved specific energy is achieved in the redox electrolyte supercapacitors.

GRAPHICAL ABSTRACT

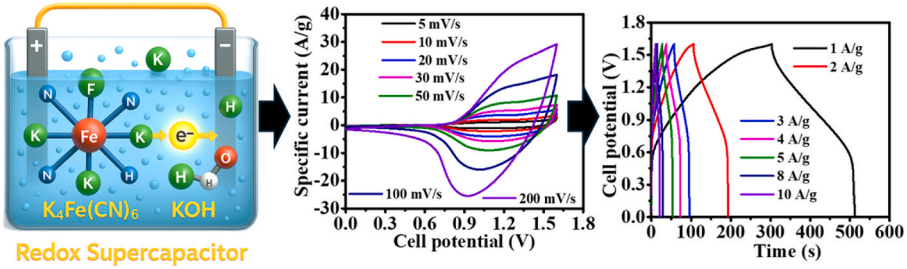

ARTICLE INFO

Keywords:
Redox electrolyte
Activated carbon
Composite material
Asymmetric supercapacitor
Specific energy
Biomass waste
Energy storage

ABSTRACT

Adding redox-active species to potassium hydroxide (KOH) enhances the electrolyte's charge storage capacity through redox reactions, thereby improving stability and broadening the potential window. This study introduces a novel mediated electrolyte with good solubility, stability, and improved reversibility. Different concentrations (0.05 M, 0.07 M, and 0.09 M) of potassium ferrocyanide (KF) were separately mixed with 3 M KOH (K3) in equal volume ratios to form the redox-active electrolytes. 0.07 M (KF70) showed superior electrochemical properties when mixed with K3. The electrolyte's ionic conductivity increased from 25.3 mS/cm for KF70 to 257.3 mS/cm after adding KF70 into K3 (K3_KF70), with a corresponding viscosity of 1.32 mPas. Hexagonal boron nitride/activated carbon composite (hBN/AC-1:0.05) electrode's specific capacity rose from 676.5C/g in K3 to 847.0C/g in K3_KF70, measured in a half-cell configuration within a potential range of 0.0–0.4 V vs. Ag/AgCl. The constructed device revealed a specific energy of 58 Wh/kg in K3_KF70, which is higher compared to 24.1 Wh/kg in K3. Additionally, the device presented a specific power of 993.7 W/kg. These results present a potential pathway for significantly enhancing specific energy in supercapacitors by facilitating additional charge storage through Faradaic redox reactions occurring within the electrolyte.

* Corresponding author.
** Corresponding author.
E-mail addresses: dejata2009@gmail.com (D.J. Tarimo), ncholu.manyala@up.ac.za (N. Manyala).

https://doi.org/10.1016/j.jpowsour.2025.238768
Received 23 August 2025; Received in revised form 10 October 2025; Accepted 3 November 2025
Available online 6 November 2025

1. Introduction

The rapid growth of the global human population is leading to an increasing energy crisis caused by higher energy demand and the depletion of fossil fuels (non-renewable sources). Continuing to depend on unclean energy leads to high pollution levels and the eventual exhaustion of these resources. Therefore, these non-renewable energy sources must be replaced by renewable energy sources, combined with energy storage devices, to create safe environments free of pollution and ensure continuous resource availability. This is because many modern electronic devices require energy storage systems that have high specific energy and power [1,2]. Therefore, focusing on energy storage systems is crucial for storing energy for future use.

Although faced with a limited supply of specific energy, supercapacitors, along with other well-known energy storage devices like batteries and fuel cells, have distinguished themselves, primarily addressing the challenge of specific energy [3,4]. The two main categories of supercapacitors are electrical double–layer capacitors (EDLCs) and pseudocapacitors [5,6]. In principle, EDLCs enable an electrostatic charge storage process, whereas a reversible Faradaic reaction occurs in pseudocapacitors. A device that combines both EDLC and pseudocapacitive behavior results in a hybrid capacitor and takes advantage of both mechanisms, leading to a system with higher specific energy and power compared to the former individual mechanisms [7–9].

The effective performance of any supercapacitor depends on the properties of the electrode and electrolyte used [10,11]. Carbon materials with EDLC behavior have a high surface area and good cycling stability. However, carbon-based supercapacitors generally have lower specific energy and shorter charge and discharge times compared to pseudocapacitors, hybrid capacitors, and batteries. Additionally, other materials, such as transition metal oxides and conducting polymers, exhibit pseudocapacitive properties, resulting in better specific capacity and energy than EDLCs [12,13].

Similarly, electrolytes provide the ions needed for ionic conduction between the two electrodes [14]. The most common liquid electrolytes include aqueous, organic, and ionic electrolytes. Aqueous electrolytes are often used because they are inexpensive, environmentally friendly, and require less manufacturing complexity [15]. In efforts to achieve better energy storage in supercapacitors, liquid electrolytes with redox species have gained interest [16].

Redox electrolytes are categorized as redox additive-liquid electrolytes, redox-active liquid electrolytes, and redox additive-polymer gel electrolytes. The redox additives include inorganic materials like potassium iodide (KI), vanadium sulfate ($VOSO_4$), nickel nitrate $(NiNO_3)_2$, ferricyanide/ferrocyanide redox couple ($K_4(CN)_6^{3-}$/ $K_4(Fe(CN)_6^{4-}$) among others, and organic materials such as indigo carmine, methylene blue, and hydroquinone (HQ) [17,18].

These redox additives are commonly added to standard electrolytes like KOH and H_2SO_4. The deposition of adsorbed ions from the electrolyte onto the electrode surface and their participation in redox processes depend on the redox species added. This leads to improved ionic conductivity and pseudocapacitance, resulting in a supercapacitor with good performance [19,20]. Some of the redox couple species reported so far include $CuSO_4$, $VOSO_4$, $Cucl_2$, $C_6H_6O_2$, $C_6H_8N_2$ KI, and $K_3Fe(CN)_6$ among others [21,22]. Herein, we focused on using potassium ferrocyanide $(K_4Fe(CN)_6)$, a water-soluble redox additive that produces K and Fe ions during charging and discharging phases, leading to enhanced electrolyte conductivity. The additive is environmentally safe, inexpensive, reversible, and chemically stable. Additionally, it can work at a varied range of concentrations, which helps in optimization whenever the best working concentrations are required with other electrolytes [23,24]. These properties make $K_4Fe(CN)_6$ contribute to enhancing the specific capacity and energy of supercapacitors [25]. Besides, $K_4Fe(CN)_6$ can be used for charge storage and serve as a redox mediator since $Fe(CN)_6^{4-}$ ions get involved in the redox reaction, where they get converted into $Fe(CN)_6^{3-}$ as described in Equation (1) [26].

$$Fe(CN)_6^{4-} \leftrightarrow Fe(CN)_6^{3-} + e^- \quad (1)$$

where Fe and CN represent iron and cyanide ions, respectively. The subscript 6 indicates that there are six cyanide ions per molecule, while the superscripts 4- and 3- signify that the ferrocyanide and ferricyanide ions have a negative charge of 4 and 3, respectively.

Recently, various researchers have added redox mediators to different electrolytes and conducted electrochemical tests to understand their impact on electrode performance. One report highlights that at 1 A/g, $NaMnPO_4$ electrode displayed a specific capacity of 92.0C/g in 2 M KOH + $K_3Fe(CN)_6$ as opposed to 66.4C/g in 2 M KOH only [27]. In another study by Sharma and Chand, at 10 A/g, the ZiF-8 electrode used obtained a specific capacity of 313.55C/g in 1 M $NaSO_4$ + 0.17 M $K_4Fe(CN)_6$ $0.3H_2O$ redox electrolyte, which is higher than 34.0C/g for the same electrode in the absence of the redox additive [26]. Besides, at 0.5 A/g, Arkhipova and coworkers, used AC in 1 M Na_2SO_4 + 0.03 M $K_3Fe(CN)_6$ and it gave a specific capacity of 320C/g, which is 3.6 times the value of the specific capacity (88.9C/g) in 1 M Na_2SO_4 [24]. Another study by Shembade et al., 2023, used a WO_3 - NF electrode which contributed a specific capacity of 360C/g at 5 A/g, in 2 M KOH +0.01 M $K_4Fe(CN)_6.3H_2O$, whereas the similar electrode deliver 328C/g in 2 M KOH electrolyte [28]. In each of the outlined studies using $K_4Fe(CN)_6$/ $K_3Fe(CN)_6$ redox additives, an improvement in specific capacity is noted, implying that the effect of redox reactions contributed to better electrode performance.

This study specifically aimed to enhance the energy storage performance of KOH using $K_4Fe(CN)_6$. The positive electrode was made with an hBN/AC-1:0.05 composite. Although hBN features strong covalent bonds, a wide band gap, and low wettability with metals [29], it offers several advantageous properties that make it a promising material for supercapacitors. These include excellent chemical and thermal stability, high resistance to corrosion, multiple ion-electrode interaction sites, and simple preparation methods [30]. Additionally, the electrode fabrication process has a significant impact on its performance. When hBN is combined with carbon to form a composite, better performance characteristics are achieved because AC has good conductivity, and its integration into hBN results in a polar covalent bond in the composite [31]. Moreover, preparing the electrode through a non-binder, simple chronoamperometric electrodeposition enhanced the adsorption and interaction of the composite particles at the working electrode surface. This particular electrode (hBN/AC-1:0.05) was used in our previous publication [32], where, in comparison to other composites, it displayed remarkable properties in 3 M KOH.

KOH is an affordable, eco-friendly inorganic compound that exhibits high ionic conductivity and low viscosity; therefore, it is used as an aqueous electrolyte in supercapacitors. However, its limited potential window and poor cycling stability reduce its specific energy, which decreases its overall reliability. As a result, adding a redox additive to 3 M KOH is expected to enhance electrode performance. The redox additive ($K_4Fe(CN)_6$) was chosen because of its good redox stability and its ability to provide additional charge storage through the Faradaic redox reaction that takes place between $K_4Fe(CN)_6$ species in KOH and hBN/AC-1:0.05, which could eventually lead to an overall improvement in electrochemical performance compared to the use of KOH alone.

This study reports, for the first time, the addition of $K_4Fe(CN)_6$ at various concentrations (0.05 M, 0.07 M, and 0.09 M) into 3 M KOH (K3). It examines its electrochemical performance in the hBN/AC-1:0.05 electrode and the fabricated device, hBN/AC-1:0.05//AC. Among all tested electrolytes (K3, K3_KF50, K3_KF70, and K3_KF90), the hBN/AC-1:0.05 electrode in K3_KF70 showed the highest specific capacity of 847.0C/g at 1 A/g in a half-cell setup with a voltage range of 0.0–0.4 V vs. Ag/AgCl. The electrode also exhibited high-rate capability, with a capacity retention of 78.4 % and a Coulombic efficiency of 99.7 %. The device further possessed a specific capacity of 210C/g, a specific energy

of 58 Wh/kg, and a specific power of 993.7 W/kg at a specific current of 1 A/g. Moreover, the device demonstrated good cyclic stability after 10,000 GCD cycles at 5 A/g, with a high Coulombic efficiency of 97.8 % and a capacity retention of 73.8 %. The low charge transfer resistance stemming from the redox-active electrolyte enhanced the electrochemical performance. These promising results confirm the potential of K3_KF70 as an ideal redox electrolyte candidate for high–performing energy storage devices. Therefore, this research provides a strategy to offer a feasible solution for enhancing the electrochemical performance of hybrid capacitors, including improved specific energy and power, rate capability, and stability, which paves the way for future innovative energy storage technology.

2. Experimental section

2.1. Reagents and material synthesis

Urea (CH_4N_2O), boric acid (H_3BO_3), potassium ferrocyanide ($K_4Fe(CN)_6$), and potassium hydroxide (KOH) were acquired from Lab Chem in Gauteng, South Africa. Nickel foam (NF) was purchased from Alantum, Munich, Germany, and deionized (DI) water (prepared using a DRAWELL laboratory purification system, available at the Department of Physics, University of Pretoria, Pretoria, South Africa). All chemicals were used without further purification.

2.1.1. Synthesis of activated carbon (AC) and hexagonal boron nitride (hBN)

The AC, hBN, and hBN/AC-1:0.05 used in this study were synthesized similarly to our previous work [32]. In summary, a dried *Eucalyptus grandis* tree bark was repeatedly washed in DI water till a neutral pH was attained. The cleaned pieces of the tree bark were thereafter dried in an electric oven for 2 h at 60 °C. Later, the samples were pre-carbonized for 2 h at 400 °C in Ar gas (300 sccm, 5 °C/min). The obtained pieces were ground into smaller particles using a mortar and pestle. Further, KOH was added to the crushed solid at a 1:1 ratio, mixed and ball-milled. The obtained fine powder was dried for 3 h in an oven at 60 °C and later activated in argon for 2 h at 700 °C (300 sccm, 5 °C/min). The obtained sample was subsequently soaked in 3 M HCl for 12 h and then cleaned using DI water through the filtration method until a pH of 7 was achieved. The end product was dried for 12 h in an electric oven at 60 °C and later used as the AC in this study.

On the other hand, hBN was prepared by mixing 2 g of boric acid (H_3BO_3), and 3 g of urea (CH_4N_2O) in a mortar and pestle for 10 min. The mixture was later ball-milled for 15 min. Afterward, it was heated for 3 h at 900 °C in nitrogen gas (300 sccm, 5 °C/min). The obtained substance was further crushed to produce hBN powder.

2.1.2. Electrode preparation and hBN/AC-1:0.05 composite

The AC electrode was prepared on a 1.0 × 1.0 cm^2 cleaned NF. The slurry was prepared by mixing a few drops of 1-methyl-2-pyrrolidone (NMP) with 80 % AC, 10 % acetylene carbon black (ACB), and 10 % polyvinylidene difluoride (PVDF). The AC sample mass loading was 3.0 mg in three-electrode measurements. For a two-electrode setup, a circular-shaped NF with an estimated radius of 1.7 cm had AC pasted on one side, serving as the negative electrode.

In preparing the hBN/AC-1:0.05 composite, 5 mg of AC and 100 mg of hBN were mixed in 100 mL of DI water. The combination was magnetically stirred for 45 min at room temperature. The prepared solution was then used to perform chronoamperometry deposition [33] at 0.45 V vs. Ag/AgCl for 60 min on each side of the NF for half-cell measurement and on a single side of the NF for full-cell measurement. Electrodeposited hBN/AC-1:0.05 composites were dried, and the deposited mass was determined. For three-electrode measurements, an average mass of 1.4 mg was achieved. A working mass ratio of m_-/m_+ of 8:1 was used to make a device of 4.6 mg/cm^2 mass, whose mass balancing was done using Equation (2) [34].

$$\frac{m_+}{m_-} = \frac{Q_+}{C_{s-}\Delta V_-} \tag{2}$$

where; m_+ is the positive electrode mass, m_- gives the negative electrode mass, Q_+ is the positive electrode charge, C_{S-} represent the specific capacitance at the negative electrode and ΔV_- stands for the voltage of the negative electrode.

2.1.3. Synthesis of aqueous redox electrolyte

Preparation of 3 M KOH (K3): 33.66 g of KOH pellets were dissolved in 200 mL of DI water and stirred magnetically till a clear, colorless solution was obtained.

Preparation of $K_4Fe(CN)_6$) additive solution: 5.3 g, 7.4 g, and 9.5 g of $K_4Fe(CN)_6$), were each dissolved in 250 mL of DI water to form 0.05 M $K_4Fe(CN)_6$ (KF50), 0.07 M $K_4Fe(CN)_6$ (KF70) and 0.09 M $K_4Fe(CN)_6$) (KF90), respectively.

Preparation of redox electrolyte: To form 3 M KOH +0.05 M $K_4Fe(CN)_6$) (K3_KF50), 3 M KOH + 0.07 M $K_4Fe(CN)_6$) (K3_KF70), and 3 M KOH + 0.09 M $K_4Fe(CN)_6$ (K3_KF90) equal volumes (15 mL) of K3 and the corresponding redox active species were mixed. Specifically, for (K3_KF50), 15 mL of K3 was combined with 15 mL of KF50, for (K3_KF70), 15 mL of K3 was combined with 15 mL of KF70, and for (K3_KF90), 15 mL of K3 was combined with 15 mL of KF90. The resulting solutions served as the aqueous redox electrolytes in this study. Fig. 1 summarizes the preparation procedure for the aqueous redox electrolyte, K3_KF70.

2.2. Material characterization

To determine the vibrational structure for AC, hBN, and hBN/AC-1:0.05, a WITec alpha 300 RAS + confocal micro-Raman microscope (Focus Innovations, Ulm, Germany) was utilized. The Raman spectrometer operated at a laser power of 2 mW and a wavelength of 532 nm, with an acquisition time of 60 s. Field Emission Scanning Electron Microscopy (FE-SEM) (Zeiss Ultra plus 55; Akishima Shi, Japan), operated at 2.0 kV, was used to examine the surface morphology of the prepared samples. The elemental composition was found using an Oxford energy-dispersive X-ray spectroscopy (EDS) system integrated within a scanning electron microscope (SEM) and operated at 20.0 kV.

The optimization of the aqueous redox electrolytes was carried out in the positive potential, 0–0.4 V vs. Ag/AgCl in a three-electrode setup using an hBN/AC-1:0.05 electrode. hBN/AC-1:0.05 served as the working electrode, glassy carbon acted as the counter electrode, and silver/silver chloride was used as the reference electrode. 30 mLs of the respective aqueous redox electrolytes were used. The cyclic voltammetry (CV) was performed at varying scan rates, ranging from 5 mV/s to 200 mV/s. The galvanostatic charge-discharge (GCD) was done for specific currents from 1 A/g to 10 A/g, while the electrochemical impedance spectroscopy (EIS) measurements were performed in Potentiostatic mode over the frequency range from 100 kHz to 10 mHz. The measurement frequencies were distributed logarithmically, with ten points per decade, yielding a total of 81 impedance data points for each experimental condition. The perturbation signal applied was a 10-mV root mean square (r.m.s.) sinusoidal waveform without any direct current (DC) offset.

3. Results and discussion

3.1. Structural analysis

Fig. 2 confirms the structural properties of the AC, hBN, and hBN/AC-1:0.05 materials. The Raman spectra obtained as indicated in Fig. 2 (a) were analyzed using the Voigt function. For AC, the D peak appeared at 1352 cm^{-1} while the G peak was at 1587 cm^{-1}. The calculated Full Width at Half Maximum (FWHM) is 141 cm^{-1} and 58

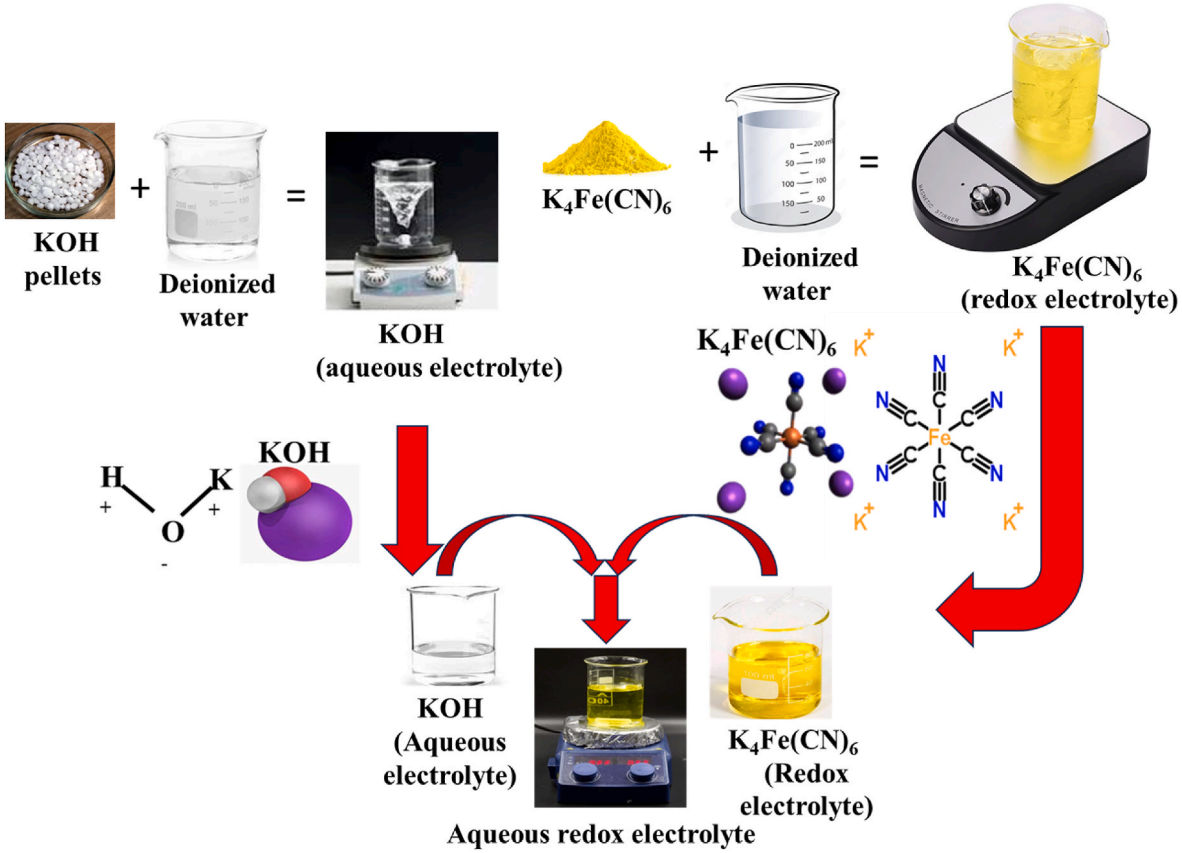

Fig. 1. The schematic diagram for the preparation of the aqueous redox electrolyte.

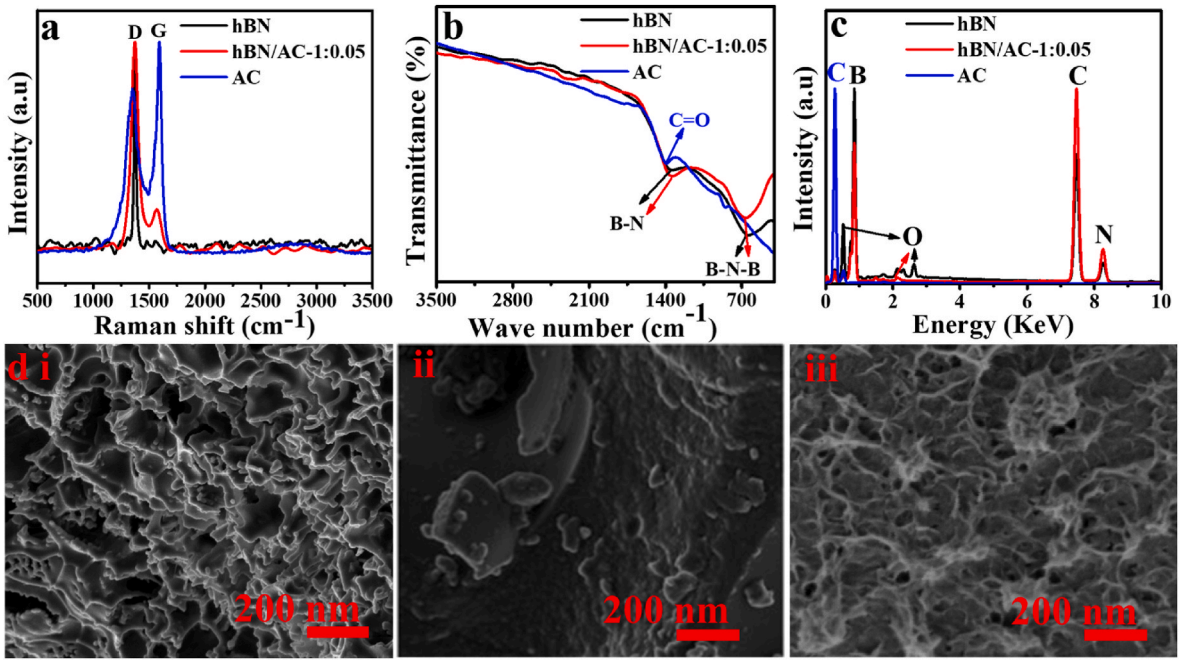

Fig. 2. (a) Raman spectra, (b) FTIR spectra, (c) EDS spectra, and (d) SEM images of (i) AC, (ii) hBN, and (iii) hBN/AC-1:0.05.

cm^{-1} for the D and G peaks, respectively. Additionally, the intensity ratio of the D and G bands (I_D/I_G) for AC is 0.85. For hBN, the E_{2g} peak appeared at 1374 cm^{-1}, while its FWHM is 21 cm^{-1}. The hBN/AC-1:0.05 composite's D and G peaks appeared at 1373 cm^{-1} and 1540 cm^{-1} positions, while their respective FWHM are at 76 cm^{-1} and 128 cm^{-1}. The 21 cm^{-1} blue shift of the D peak for the hBN/AC-1:0.05 composite compared to AC indicates an interaction between hBN and AC, resulting in a hBN/AC-1:0.05 composite with structural modification at the carbon sites. Additionally, the 47 cm^{-1} red shift in the G band for the hBN/AC-1:0.05 composite compared to AC indicates that the formation of the

hBN/AC-1:0.05 composite introduced tensile strain and increased disorder in the AC structure. This suggests a strong interaction and structural modification, confirming successful hybridization between hBN and AC [35]. The hBN/AC-1:0.05 composite's intensity ratio of the D and G bands (I_D/I_G) is 0.89. The higher intensity ratio in the hBN/AC-1:0.05 composite (0.89) vs. AC (0.85) suggests more defects, vacancies, increased structural disorder, and reduced graphitic crystallinity in the composite [36]. This is mainly due to the incorporation of hBN into the carbon matrix, which aligns with the observed peak shifts. The created localized states allow electron movement across the interface, enabling electron conduction. The composite interface further aids in ion diffusion. This occurs when the highly polar sites on the hBN surface attract ions, facilitating their movement from regions of high concentration to regions of low concentration. Again, the micropores/mesopores afforded by the presence of AC in hBN provide ion transport pathways, hence ion diffusion.

Moreover, FTIR measurement in Fig. 2 (b) shows the presence of carbon and oxygen atoms in AC, while hBN and hBN/AC-1:0.05 composite have an alternating sublattice of boron and nitrogen atoms. hBN structure has an estimated lattice mismatch of 1.7 %, making hBN display a flat atom surface connected with few dangling bonds and defects [37]. Fig. 2 (c) illustrates the EDS spectra for AC, hBN, and hBN/AC-1:0.05 and the respective elements in each sample. AC contains C (88.8 %) and O (11.2 %). The hBN has C (31.4 %), O (31.9 %), B (32.5 %), and N (4.2 %), while hBN/AC-1:0.05 possesses C (57.8 %), O (7.5 %), B (29.3 %), and N (5.4 %). In addition, Fig. 2 (d) shows the SEM images for (i) AC, (ii) hBN, and (iii) hBN/AC-1:0.05. The AC sample displayed an interconnected porous material, whereas hBN exhibited overlapping films with wrinkles and folds. Moreover, hBN/AC-1:0.05 presented holes and folded overlying layers. The Raman, EDS, and SEM images on the composite confirm that the hBN/AC-1:0.05 composite contains combined characteristics of both AC and hBN.

The confirmed hBN/AC composite structure provides better performance than using hBN or AC separately. The hybridized composite has a synergy from the high surface area of AC and defect-mediated pseudocapacity from hBN. Additionally, there are electrostatic interactions through the polar nature of hBN, which aid in the adsorption and stabilization of the redox-active charged species ($Fe(CN)_6^{4-/3-}$). Further, the structure of the composite (hBN/AC) provides defect sites and a heterojunction effect, which enhances charge transfer due to a lowered activation barrier. The hBN layered structure also prevents pore blockage in AC, allowing more channels for ion diffusion of the electrolyte into the carbon pores [38]. This ensures effective interaction between AC and the redox electrolyte used in this study, which is not limited to the surface alone.

3.2. Electrolytes characterization

To better understand how the transport properties of the electrolytes impact supercapacitor performance, we plotted bar graphs showing the ionic conductivity and viscosity of the as-prepared electrolytes, as illustrated in Fig. 3(a and b).

More details on the electrolyte properties, including pH, ionic conductivity, and viscosity, are provided in Table 1. Regarding the electrolyte pH, all the redox additives, aqueous and redox-mediated electrolytes, were alkaline. The values ranged from 9.15, 9.22, 9.35, and 13.85 (correct to 2 decimal places) for KF90, KF70, KF50, and K3, to 13.84, 13.81, and 13.77 (correct to 2 decimal places) for K3_KF90, K3_KF70, and K3_KF50, respectively. In terms of electrolyte ionic conductivity, the obtained values were written to 1 decimal place, where K3 had the highest value at 520.0 mS/cm. The redox-active electrolytes KF50, KF70, and KF90 had ionic conductivities of 21.1, 25.3, and 37.2 mS/cm, respectively. The ionic conductivity improved with an increase in $K_4Fe(CN)_6$ concentration because of the availability of more conduction ions. After combining K3 with respective redox additive electrolytes (KF50, KF70, and KF90), the electrolytes' ionic conductivities recorded were 266.9, 257.3, and 286.7 mS/cm for K3_KF50, K3_KF70, and K3_KF90, respectively. Further, these results indicate that the combination of K3 and $K_4Fe(CN)_6$ (KF50, KF70 & KF90) led to an increase in the availability of more conducting ions and improved the ionic conductivity of aqueous redox electrolytes. Moreover, the interaction between K3 and the respective quantity of $K_4Fe(CN)_6$ contributed to improvement in ionic conductivity since K3 serves as a carrier donor of K^+, hence better ionic conductivity [39].

Besides, as indicated in Fig. 3 (b), for the redox active species electrolyte, as the concentration of $K_4Fe(CN)_6$ amplified, the viscosities were recorded to 2 decimal places as 0.97, 1.03, and 1.07 mPas for KF50, KF70, and KF90, respectively. In comparison, K3 had a viscosity of 1.85

Table 1
Properties of the as-prepared electrolytes (K3: 3 M KOH, KF50: 0.05 M $K_4Fe(CN)_6$ KF70: 0.07 M $K_4Fe(CN)_6$), KF90: 0.09 M $K_4Fe(CN)_6$), K3_KF50: 3 M KOH + 0.05 M $K_4Fe(CN)_6$), K3_KF70: 3 M KOH + 0.07 M $K_4Fe(CN)_6$) and K3_KF90: 3 M KOH + 0.09 M $K_4Fe(CN)_6$).

S/No.	Electrolyte identity	Electrolyte pH	Electrolyte ionic conductivity (mS/cm)	Electrolyte viscosity (mPas)
1	K3	13.88	520.0	1.85
2	KF50	9.35	21.1	0.97
3	KF70	9.22	25.3	1.03
4	KF90	9.15	37.2	1.07
5	K3_KF50	13.77	266.9	1.79
6	K3_KF70	13.81	257.3	1.32
7	K3_KF90	13.84	286.7	1.12

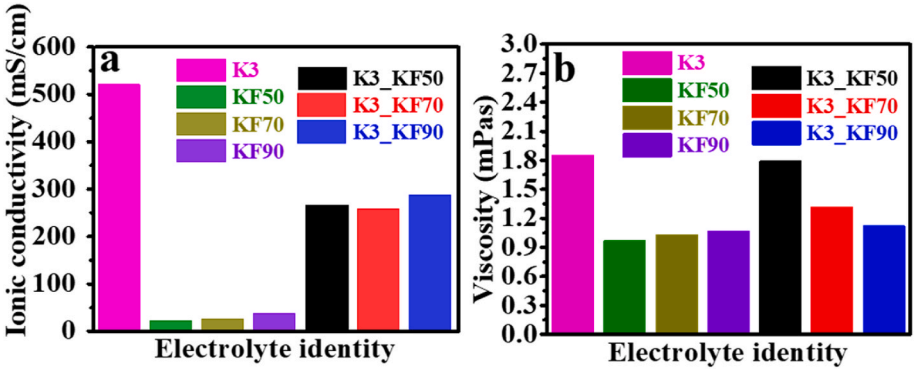

Fig. 3. Graphical representation of (a) ionic conductivity, (b) viscosity of the as-prepared electrolytes for K3, K3_KF50, K3_KF70, and K3_KF90. (The abbreviations used stand for KF50: 0.05 M $K_4Fe(CN)_6$), KF70: 0.07 M $K_4Fe(CN)_6$), and KF90: 0.09 M $K_4Fe(CN)_6$).

mPas. After combining redox-active species with K3, the viscosity decreased with an increase in redox-active species. K3_KF50, K3_KF70, and K3_KF90 had viscosities of 1.79 mPas, 1.32 mPas, and 1.12 mPas, respectively. The decrease in viscosity with increasing ionic conductivity showed that more viscous electrolytes interfered with ion transfer, while less viscous electrolytes promoted ion movement [40,41].

3.3. Electrochemical analysis

3.3.1. Three-electrode analysis

The evaluation of the three-electrode system provides insights into electrochemical behavior and helps identify the optimal electrolyte (Fig. 4(a–f)). Fig. 4 (a) displays the cyclic voltammetry (CV) of hBN/AC-1:0.05 in K3, K3_KF50, K3_KF70, and K3_KF90 at a scan rate of 30 mV/s within a potential window of 0.0–0.4 V vs. Ag/AgCl. The CV curves of the hBN/AC-1:0.05 electrode display Faradaic activity with enhanced electrochemical performance in aqueous redox electrolytes (K3_KF50, K3_KF70, and K3_KF90) compared to the aqueous electrolytes (K3). This suggests that fast and efficient electron transfer reactions happen at the electrode surface between the redox species [42]. The sample in K3_KF70 exhibited the highest current response compared to K3_KF50 and K3_KF90, emphasizing its enhanced Faradaic performance. Fig. 4 (b) presents non-linear GCD traces for hBN/AC-1:0.05 in K3 and the aqueous redox electrolytes at 1 A/g, in 0.0–0.4 V vs. Ag/AgCl potential

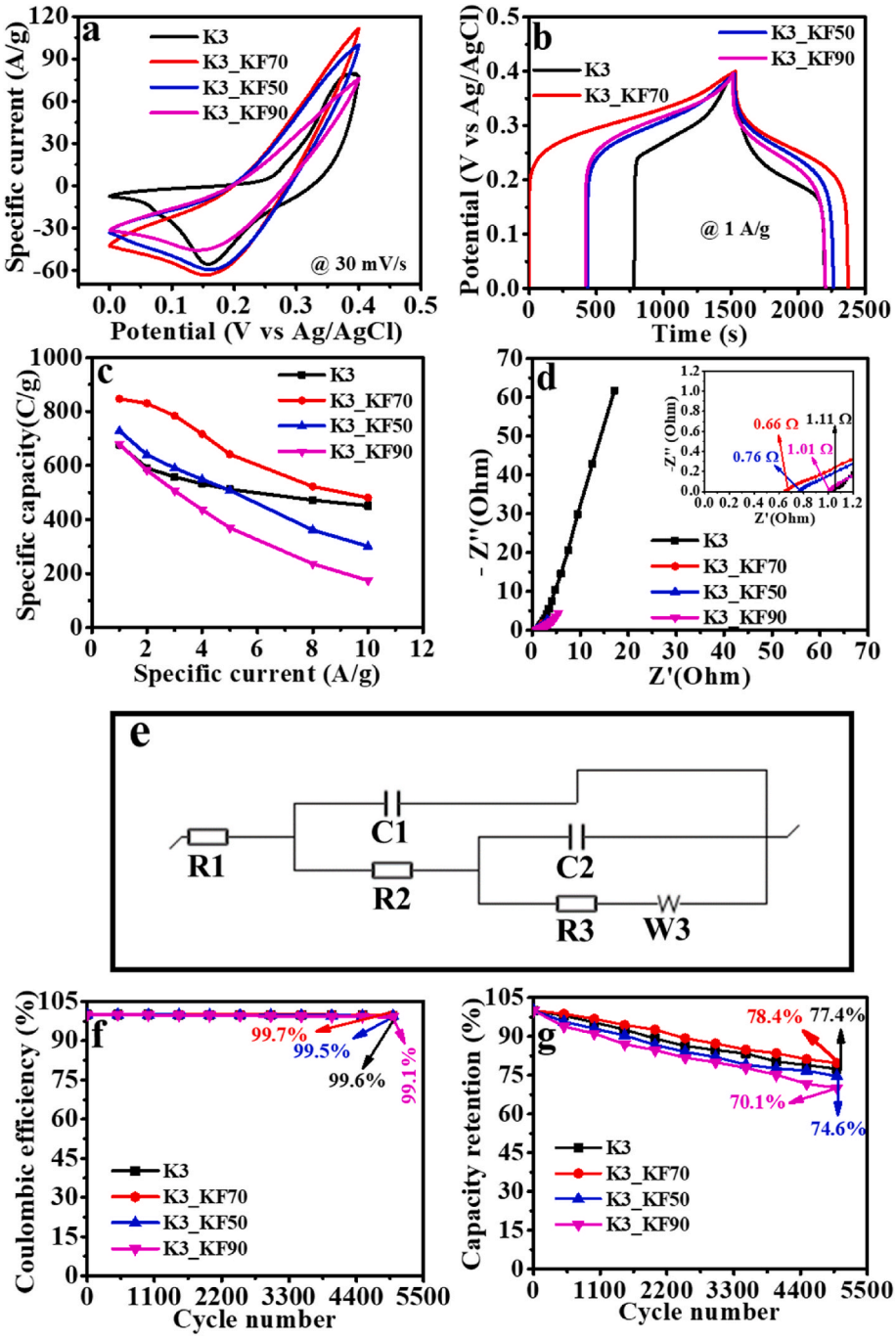

Fig. 4. (a) CV curves, (b) GCD curves, (c) specific capacity vs. specific current, (d) EIS Nyquist plot, (e) the equivalent circuit used to fit the redox electrolytes' EIS curve data, (f) Coulombic efficiency vs. cycle number, and (g) capacity retention vs. cycle number for hBN/AC-1:0.05 in the electrolytes. (The abbreviations used stand for K3: 3 M KOH, K3_KF50: 3 M KOH + 0.05 M $K_4Fe(CN)_6$, K3_KF70: 3 M KOH + 0.07 M $K_4Fe(CN)_6$ and K3_KF90: 3 M KOH + 0.09 M $K_4Fe(CN)_6$).

window. The results are consistent with the CV characteristics in Fig. 4 (a). During the electrochemical process at the electrode-electrolyte interface, the redox reaction occurs due to the generated ferro-/ferricyanide redox couple $\left[\left(Fe^{2+}(CN)_6\right]^{4-}/\left[\left(Fe^{3+}(CN)_6\right]^{3-}\right.\right.$, leading to an improvement in the overall electrochemical performance for redox-mediated electrolytes. The reaction that occurs during this process is as indicated in Equation (3) [24].

$$[K_4Fe(CN)_6]^{4-} \leftrightarrow [K_4Fe(CN)_6]^{3-} + e^- \quad (3)$$

hBN/AC-1:0.05 in K3_KF70 has the longest charge-discharge time compared to K3 and the other redox electrolytes. This suggests that the K^+ and OH^- ion interacts best with the concentration of 0.07 M (K3_KF70) for the redox additive when compared to the other concentrations of 0.05 M and 0.09 M.

The specific capacities for the hBN/AC- 1:0.05 electrode in the four electrolytes in each specific current were calculated using Equation (4) [32].

$$Q_s\ [C\ g^{-1}] = \frac{I \times t}{m} \quad (4)$$

where Q_s represents the electrode's specific capacity, I (mA) stand for the current, t (s) indicates the discharge time, and m (mg) is the mass of the active material.

Moreover, the specific capacity versus the specific current for the electrode in the respective electrolytes is shown in Fig. 4 (c). The results show that the electrode in K3_KF70 had the highest specific capacity of 847.00C/g, followed by K3_KF50 at 727.95C/g and K3_KF90 at 680.09C/g at 1 A/g. The specific capacity for hBN/AC-1:0.05 in K3 (676.50C/g) was lower than in all the aqueous redox electrolytes at lower specific currents. However, K3 maintained a better specific capacity than K3_KF50 and K3_KF90 at higher specific currents. This is because K3 has slow redox kinetic reactions during charge storage and cannot match the faster kinetic reactions enhanced by redox species at a lower specific current in K3_KF50, K3_KF70, and K3_KF90. At high specific currents, K3_KF50 and K3_KF90 experienced high polarization and incomplete charge utilization, leading to a rapid decrease in specific capacity compared to K3 and K3_KF70, thus limiting ion diffusion at the electrode/electrolyte interface [43]. Furthermore, the hBN/AC-1:0.05 electrode in K3_KF70 had better specific capacities than in K3 for lower and higher specific currents. This further confirms the good performance of the hBN/AC-1:0.05 electrode in K3_KF70 compared to the other electrolytes. Additionally, there was a decrease in rate capability with an increase in specific current, indicating restricted distribution of electrolyte ions into the electrode [44]. The rate capability values were 67 %, 57 %, 41 % and 26 % for K3, K3_KF70, K3, KF50 and K3_KF90, respectively. The outcomes further designate that the introduction of the redox additive in K3 further enhanced the specific capacity of each aqueous redox electrolyte, giving them the capability of displaying a specific capacity greater than the hBN/AC-1:0.05 electrode in K3 (676.50C/g) at a lower specific current and maintaining the highest specific current for K3_KF70 (847.00C/g) at 1 A/g.

EIS was conducted to enhance the understanding of ion diffusion in the respective electrolytes and the charge transfer behavior of the electrode material, as illustrated in Fig. 4 (d). The inset shows the enlarged portion of the high-frequency range. From the graph, the hBN/AC-1:0.05 electrode in K3 had the most extended diffusion length compared to its performance in all the other electrolytes. The same electrode in K3_KF70 exhibited the shortest diffusion length, followed by its performance in K3_KF50, while the electrode in K3_KF90 had a comparatively longer diffusion length. This implied that the electrode in K3_KF70 had the lowest equivalent series resistance (ESR) due to the fast redox reaction. Furthermore, the slope of hBN/AC-1:0.05 in K3_KF70 is nearer to the imaginary impedance axis, as indicated by the inset, in contrast to the same electrode in all other electrolytes, indicating rapid ion diffusion kinetics on the electrode surface. This behavior confirms that hBN/AC-1:0.05 in K3_KF70 demonstrates a rapid charge transfer and electrolyte ion diffusion rate. Besides, the ESR of the electrode in the electrolytes is 0.66 Ω for K3_KF70, 0.76 Ω for K3_KF50, 1.01 Ω for K3_KF90, and 1.11 Ω for K3. The low ESR value for the electrode in K3_KF70 further confirmed the superior specific capacity of the electrode in K3_KF70 compared to K3_KF50, K3_KF90, and K3, as observed in Fig. 4 (c). On the other hand, an increase in the concentration of $K_4Fe(CN)_6$) beyond 0.07 M, which is 0.09 M, led to "ion crowding", which restricted the movement of ions and reduced the electrolyte's overall conductivity. This results in an increase in internal resistance, leading to a decrease in capacity and further limiting the energy storage capability [45].

Additionally, considering the relationship between the Warburg element and diffusion coefficients of hBN/AC-1:0.05 in the aqueous redox electrolytes, Equations (5) and (6) [46] were used.

The Warburg impedance is given by Equation (5);

$$Z_W(j\omega) = \frac{\sigma}{\sqrt{j\omega}} \quad (5)$$

Where Z_W is the Warburg impedance (Ω), σ represents the Warburg coefficient ($\Omega.s^{½}$), jω is the Laplace variable, where j is the imaginary unit, and ω stands for angular frequency (rad/s).

A redox process involving diffusion of electroactive species is represented by Equation (6);

$$\sigma = \frac{RT}{n^2F^2AC\sqrt{2D}} \quad (6)$$

where R is the gas constant (8.314 J mol^{-1} K^{-1}), T is the absolute temperature (K), n is the number of electrons transferred, F represents the Faraday constant (96485 C mol^{-1}), A is the electrode area (cm^2), C is the bulk concentration of the redox species (mol/cm^3), and D is the diffusion coefficient (cm^2/s).

Equation (6) implies that the **Warburg coefficient is inversely proportional to the square root of the diffusion coefficient.** That is, a higher σ means slower diffusion, and a lower σ means faster diffusion. This is further confirmed by the data obtained after the EIS fitting of the composite electrode in the redox-active electrolytes. From the equivalent fitting circuit obtained in Fig. 4(e), which was similar for the three redox electrolytes, the data in Table 2 were derived. The value of σ obtained for K3_KF90 is 0.80 $\Omega\ s^{½}$, followed by K3_KF50 at 0.70 $\Omega\ s^{½}$ and lastly K3_KF70 at 0.58 $\Omega\ s^{½}$. These values confirm that K3_KF70 had the fastest diffusion, while K3_KF90 experienced the least diffusion.

Moreover, Fig. 4 (f and g) displays the Coulombic efficiency and capacity retention against the cycle number at 5 A/g, calculated using Equations (7) and (8) [9], respectively. The hBN/AC-1:0.05 electrode in K3_KF70, K3_KF50, K3_KF90 and K3 exhibited Coulombic efficiencies of 99.7 %, 99.5 %, 99.1 %, and 99.6 %, respectively. The hBN/AC-1:0.05 electrodes in respective electrolytes displayed capacity retention of 78.4 %, 74.6 %, 70.1 %, and 77.4 % for K3_KF70, K3_KF50, K3_KF90, and K3, respectively, after 5000 GCD cycles.

$$C_E\ [\%] = \frac{t_D}{t_C} \times 100 \quad (7)$$

$$C_R\ [\%] = \frac{t_{DN}}{t_{D1}} \times 100 \quad (8)$$

where C_E is the Coulombic efficiency, $t_{D,}$ and t_C indicate the time used

Table 2
Fitted circuit elements and their respective values.

Elements	R1 (Ω)	C1 (F)	R2 (Ω)	C2 (F)	R3 (Ω)	σ ($\Omega.s^{½}$)
K3_KF50	1.49	0.0054	0.31	0.068	0.49	0.70
K3_KF70	1.59	0.0044	0.13	0.079	0.26	0.58
K3_KF90	1.64	0.0030	0.27	0.048	0.43	0.80

for discharge and charge, respectively. C_R is the capacity retention, while t_{D1} and t_{DN} are the discharge times after the first and N^{th} cycles, respectively.

Based on the discussion in Table 1, Figs. 3 and 4, and Table 2, the low electrochemical performance experienced in K3 was mainly attributed to its high viscosity and low diffusion-controlled process, although it had the highest ionic conductivity compared to the redox-mediated electrolytes. Although K3_KF90 had an ionic conductivity of 286.7 mS/cm and a low viscosity of 1.12 mPas, it experienced a rapid decline in specific capacity with an increase in specific current. This is confirmed in Fig. 4 (c) and Table 2, resulting in its performance being lower than that of K3_KF50 and K3_KF70. The good ionic conductivity of 257.3 mS/cm and low viscosity of 1.32 mPas for K3_KF70 contributed to its good electrochemical performance. This is further confirmed by the hBN/AC-1:0.05 electrode performance in K3_KF70, which exhibits a good and stable specific capacity with an increase in specific current (Fig. 4 (c)). Hence, K3_KF70 was chosen as the optimum electrolyte and used for further measurements.

The electrochemical performance of the as-prepared electrode (hBN/AC-1:0.05) in K3_KF70 is further presented in Fig. 5. The CV patterns shown in Fig. 5 (a) display Faradaic behavior within 0.0–0.4 V vs. Ag/AgCl for scan rates from 5 to 200 mV/s. The area under the CV curves increased with an increase in scan rate, resulting in a high current response due to the fast charge transfer kinetics at the electrode surface. Besides, as the scan rate increased, the Faradaic peak shapes significantly reduced due to a fast interaction rate, leading to less ion interaction with the electrode [47,48]. The GCD plot in Fig. 5 (b) shows non-linear curves supporting the Faradaic characteristics on the CV curves in Fig. 5 (a). At low specific currents, the interaction time for $Fe(CN)_6^{4-}$ ions with the electrode's interface are sufficient. This yields higher specific capacity values than the lower specific capacity obtained at higher specific currents. At high specific currents, very fast interaction occurs between the ions and the electrode at the interface, leading to incomplete reversible capacity. OH^- ions from KOH provide high ionic conductivity, which reduces the overall internal resistance and improves the rate capability. Additionally, the OH^- ions aid in stabilizing the oxidized/reduced form of ferro/ferricyanide, improving redox reversibility and electrochemical performance [49,50]. Besides, understanding the charge storage mechanism of any electrolyte is essential because it affects supercapacitor performance. The power law, as expressed in Equations (9) and (10) [51] was used to provide clear information on the energy storage mechanism and charge storage contributions in this study.

$$I(V) = av^b \tag{9}$$

$$Log\, I(V) = a + b\, log\, v \tag{10}$$

where $I(V)$ is the peak current for a specific scan rate, a and b are constants that can be obtained from the relationship between $Log\, I(V)$ and $log\, v$. a is the y-intercept, while b is the slope of the graph. If the value of b equals 1, the charge storage mechanism is a surface–controlled process, and if b equals 0.5, then the storage mechanism is diffusion-controlled. Fig. 5 (c) displays a plot of $Log\, I(V)$ versus $log\, v$. The estimated value of b is 0.61 and 0.67 for the anodic and cathodic processes, respectively. The obtained values range from 0.5 to 1, indicating that both surface- and diffusion-controlled processes are involved in the charge storage mechanism. However, the diffusion-controlled process dominates in the charge storage because the b values obtained are closer to 0.5 as opposed to 1.

Moreover, the capacitive and diffusion–controlled contribution was determined using Equations (11) and (12) [33].

$$I\,(V) = K_1 V + K_2 v^{0.5} \tag{11}$$

$$\frac{I(V)}{v^{0.5}} = K_1 v^{0.5} + K_2 \tag{12}$$

where, $K_1 V$ and $K_2 v^{0.5}$ are capacitive and diffusion-controlled contributions, respectively. K_1 *and* K_2 are the slope and y-intercept determined by plotting $\frac{I(V)}{v^{0.5}}$ vs $v^{0.5}$.

Fig. 5 (d) shows the capacitive and diffusion-controlled contribution for hBN/AC-1:0.05 in K3, K3_KF50, K3_KF70, and K3_KF90,

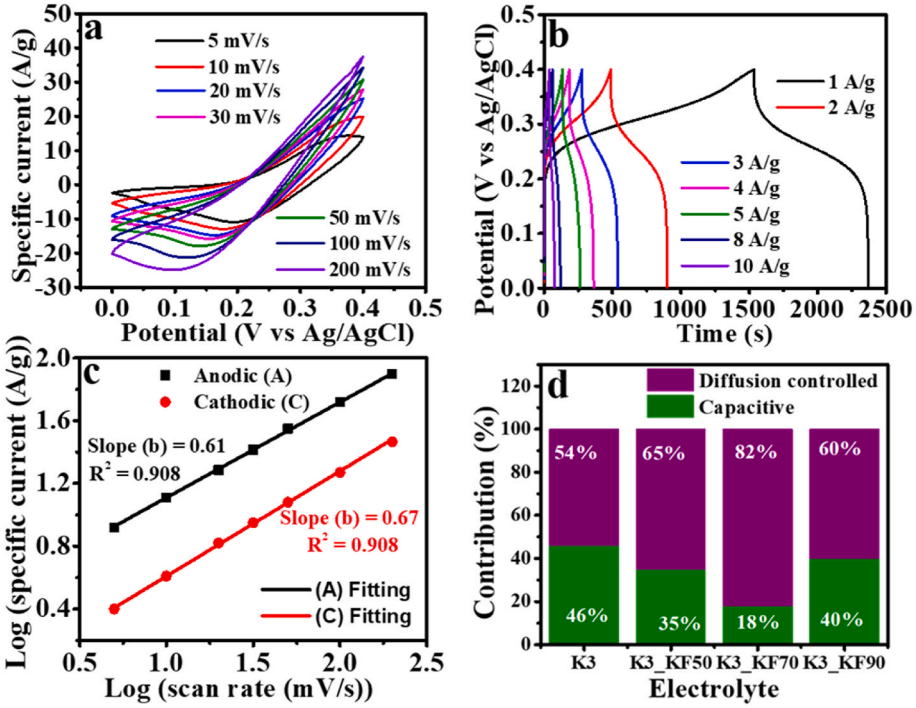

Fig. 5. (a) CV traces, (b) GCD traces, (c) the relationship of log current versus log scan rate (power law-cathodic and anodic for hBN/AC-1:0.05 in K3_KF70, and (d) contribution (%) of capacitive and diffusion-controlled charge storage for hBN/AC-1:0.05 in K3, K3_KF50, K3_KF70, and K3_KF90.

respectively, at 5 mV/s. The bar graph illustrates the charge storage mechanisms with their respective percentages. These results showed that the diffusion-controlled process dominated in K3_KF70, which displayed the highest value (82 %), followed by K3_KF50 (65 %), K3_KF90 (60 %), and K3 (54 %). On the other hand, hBN/AC-1:0.05 in K3 displayed the highest capacitive contribution (46 %), followed by K3_KF90 (40 %), K3_KF50 (35 %), and K3_KF70 (18 %). Consequently, KF50, KF70, and KF90 contributed 11 %, 28 % and 6 %, respectively. The diffusion-controlled process was highly enhanced in the aqueous redox electrolytes because of the redox additives' species.

Table 3 presents comparative data on the specific capacity of positive electrodes from three-electrode measurements with similar half-cells reported in the literature. The table further indicates that, in comparison to other redox electrolytes used in recent studies, the current redox electrolyte, K3_KF70, demonstrated the highest specific capacity of 847.0C/g at 1 A/g.

The electrochemical performance of AC in K3_KF70 is demonstrated in Fig. 6(a–d). The AC electrode's electrochemical performance was evaluated at negative potentials because its primary charge storage mechanism is anion adsorption at the electrode surface, which is more efficient at negative than positive potentials. In Fig. 6 (a), the CV traces of the electrode in K3_KF70 displayed non-linear rectangular shapes. The presented CV curves exhibited more EDLC-like behavior at lower scan rates and more pseudocapacitive behavior at higher scan rates. The area under the curve for the CV traces improved with an increase in scan rate, which signified that the capacitive current component was dominant over the Faradaic current. Furthermore, the electrolyte's redox reactions increased the potential window, as they provided an additional charge storage mechanism beyond the typical EDLC [56]. The electrode optimal working voltage window changed from - 0.7 to 0.0 V while in K3, as shown in our previous study [32], to −1.0 to 0.0 V when used in K3_KF70 (this study). The GCD curves, which are nearly isosceles triangle-shaped, are displayed in Fig. 6 (b). The traces confirm charge storage mechanisms shown in Fig. 6 (a). Moreover, as the specific current increased from 1 A/g to 10 A/g, the area under the curve decreased, implying low specific capacitance. Fig. 6 (c) shows the specific capacitance (F/g) against the specific current of the AC electrode in K3_KF70. The specific capacitance is reduced with an increase in specific current. This behavior shows that at high specific currents, the time taken for charging and discharging is shorter as opposed to the time spent at low specific currents. At 1 A/g, the electrode had a specific capacitance of 95.08 F/g. To understand the charge mobility within the AC electrode in K3_KF70, the EIS measurement was carried out in an open-circuit potential at a frequency range of 100 kHz to 10 mHz, and the results are displayed in Fig. 6 (d). A nearly vertical curve was displayed at low frequency, showing good ionic diffusion with an ESR value of 0.91 Ω, hence, low resistance. The ESR is a component of the ionic resistance of the electrolyte, the intrinsic resistance of the electrode, and the contact resistance between the electrode and the current collector interface [54]. Besides, the obtained Nyquist plot had a barely noticeable semicircle at the high-frequency region, which indicated minimal charge transfer resistance (R_{CT}), confirming faster adsorption/desorption during charge/discharge, and enabling better electrochemical performance.

3.3.2. two-electrode analysis

The previously discussed hBN/AC-1:0.05 composite and AC electrodes were assembled as the positive and negative electrodes, respectively, to make an asymmetric device. Equation (2) was used to determine the mass balancing for the device whose mass was 4.6 mg/cm^2, with an 8:1 working mass ratio (m_-/m_+). The designed device was tested under a two-electrode setup in an electrochemical workstation using a K3_KF70 aqueous redox electrolyte due to its superior performance as compared to the rest of the other electrolytes tested. The CV traces for the individual electrodes are shown in Fig. 7 (a). The curves for the negative electrode were recorded from −1.0 to 0.0 V vs. Ag/AgCl, while the positive electrode was recorded from 0.0 to 0.4 V vs. Ag/AgCl. Additionally, the negative electrode exhibited EDLC behavior, while the positive electrode displayed Faradaic behavior. The nature of the asymmetric device CVs arises from the combined EDLC properties of AC in the negative electrode and the Faradaic properties of hBN/AC-1:0.05 in the positive electrode in an aqueous redox electrolyte. Here, a noteworthy contribution arises from the current response of the positive electrode, thereby highlighting the Faradaic nature of the CV in the system. The assembled device's CV curves were further recorded at scan rates between 5 mV/s and 200 mV/s, in a cell potential fixed from 0.0 to 1.6 V, as illustrated in Fig. 7 (b). Moreover, the CV traces had similar shapes at varied scan rates, indicating fast and good electrochemical reversibility at the electrode-electrolyte interface. Additionally, the CV curve area increased with a rise in scan rate, indicating that the device had a high current response. Similar CV behavior was observed in other asymmetric devices like in a mixed metal oxide loaded multiwalled carbon nanotube using redox additive electrolyte (1 M KOH + 0.1 M $K_4Fe(CN)_6$ and 1 M Na_2SO_4+0.1 M $K_4Fe(CN)_6$) [19]. Another example showing similar properties is an integrated Co(OH)F nanorods and layered $Ti_3C_2T_x$ in 3 M KOH + 0.5 M LiOH redox electrolyte [57].

On the other hand, the GCD study was conducted to analyze the assembled device's charge storage capability, for which the curves were recorded at specific currents ranging from 1 A/g to 10 A/g, as shown in Fig. 7 (c). The GCD curves were non-linear and showed combined EDLC and pseudocapacitive characteristics of the assembled device, similar to those displayed by CV curves in Fig. 7 (b). The GCD curves' discharge time decreased as the specific currents increased, signifying a decrease in ion diffusion and, hence, less charge storage at elevated specific currents. The specific capacity of the fabricated device was calculated using the discharging time from the GCD curves, as shown by Equation (4). The specific capacity against the specific current for the device is displayed in Fig. 7 (d). The device had a specific capacity of 210.0C/g, 176.3C/g, 155.2C/g, 142.1C/g, 130.3C/g, 113.5C/g, and 103.8C/g at 1, 2, 3, 4, 5, 8, and 10 A/g, respectively. Additionally, its rate capability was 50 %. This is because of the electrons and ions transport resistance caused by the underutilization of inner pores within the electrode, since the interaction is mainly at the surface. Again, the charge transfer kinetics within the redox electrolyte decrease, and, at this stage, only macropores and mesopores participate in ion transportation while micropores go dormant. As displayed by the curve in Fig. 7 (d), the specific capacity decreased with an increase in specific current. This behavior occurs due to minimal interaction time between the electrode and electrolyte ions at a high specific current.

To further validate the results obtained, a Ragone plot, shown in

Table 3
Comparative table showing the specific capacity contribution of positive electrodes in different redox electrolytes in a half-cell configuration.

S/No	Positive electrode	Redox electrolyte	Potential window (V)	Specific capacity (C/g)	Specific current (A/g)	Ref.
1	$NaMnPO_4$	2 M NaOH + $K_3Fe(CN)_6$	−0.5–0.3	92.0	1	[27]
2	rGO	1M H_2SO_4 + TACBQ	−0.2–0.8	358.0	1	[52]
3	AC-based	1 M Na_2SO_4 + 0.03 M $K_3Fe(CN)_6$	0.0–0.8	320	0.5	[24]
4	rGO	0.1 M Na_2MoO_4 + 1 M Li_2SO_4	−1–0.8	362.7	0.5	[53]
5	CO3O4/Polyaniline/graphene	1 M Na_2SO_4 + 0.075 M KI	−0.8–0.8	761.6	1	[54]
6	$SnO_2 - La_2O_3$	3 M KOH + 0.2 M $K_3[Fe(CN)_6]$	−0.3–0.7	637	1	[55]
7	**hBN/AC-1: 0.05**	K3_KF70	**0.0–0.4**	**847.0**	**1**	**This Work**

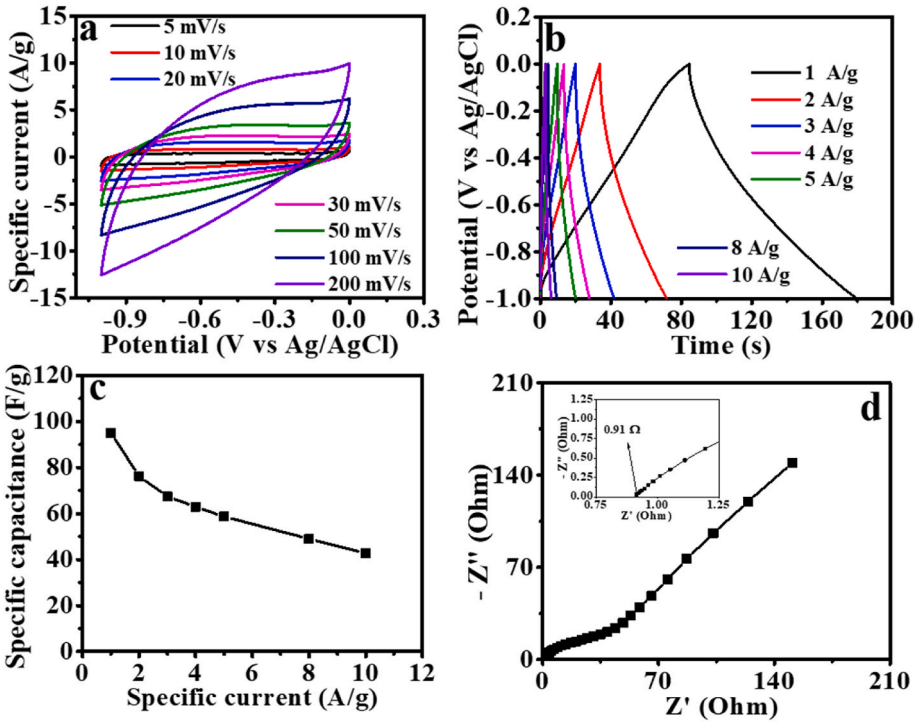

Fig. 6. (a) CV curves, (b) GCD curves, (c) Specific capacitance vs. specific current, and (d) EIS Nyquist plot for AC in K3_KF70.

Fig. 7 (e), presents the specific energy versus specific power of the current study in comparison with similar devices from the literature. The specific energy and power were calculated using Equations (13) and (14) [33], respectively. The results showed that the obtained device had a maximum specific energy of 58.0 Wh/kg with a specific power of 993.7 W/kg, at 1 A/g. The specific energy of the obtained device (58.0 Wh/kg) is 2.4 times better than that of the same device assembled in K3 (24.1 Wh/kg), as reported in our previous study [32]. It is worth noting that the specific energy and specific power of the redox electrolyte-enhanced hybrid capacitors are comparable to or superior to those of similar devices reported, as shown in Table 4.

The stability of the fabricated device was analyzed using the device's Coulombic efficiency (%) and capacity retention (%) as a function of cycle number. The measurements were analyzed for constant 10,000 GCD cycles, as displayed in Fig. 7 (f). The device exhibited a Coulombic efficiency of 97.8 % and a capacity retention of 73.8 % after 10,000 GCD cycles at 5 A/g. The good Coulombic efficiency and cycling stability also demonstrate that the developed supercapacitor has great potential for practical applications.

$$E_s\left[\mathrm{Wh\,kg^{-1}}\right] = \frac{I}{3.6\,m}\int_0^V V(t)dt \tag{13}$$

$$P_s\left[\mathrm{W\,kg^{-1}}\right] = 3600\,\frac{E_s}{\Delta t} \tag{14}$$

where, E_s, denotes the specific energy, P_s, stands for the specific power, I (mA) is the current, m (mg) is the total mass of the active material, $\int V(t)\,dt$ and Δt (s) shows the integral under the discharge curve and discharge time, respectively.

Fig. 8 (a) (i) and (b) (i) show the morphology of the positive and negative electrode before cycling, while (a) (ii) and b (ii) display the morphology after stability. The SEM images before cycling display a uniform distribution of interconnected porous layers of hBN/AC-1:0.05, while AC appears porous. After 10,000 cycles, the electrode's surface became rough and partially collapsed, showing pore blockage and particle agglomeration. This suggests structural degradation, hence the observed decrease in capacity retention in Fig. 7 (f). The Nyquist plot of the EIS data, with the fitting using the equivalent circuit displayed in Fig. 8 (d) curve is shown in Fig. 8 (c). The graph shows a curve that diverges from the y-axis within the low-frequency area, which indicates the dominance of diffusive capacity behavior [64,65] of the assembled device. The EIS curve results agree with Fig. 5 (d), which suggests that the K3-KF70 charge storage mechanism is primarily diffusion-controlled (82 %) as opposed to a capacitive charge storage mechanism (18 %). The equivalent circuit used to fit the data in Fig. 8 (c) gives an equivalent series resistance (Rs = 5.88 Ω) that is in series with the other elements in the circuit (R_{CT}, C_1, Q, R_{L1}, W, C_2 & R_{L2}). In the high-frequency region, charge transfer resistance (R_{CT} = 2.08 Ω) is parallel to the real capacitance (C_1 = 0046 F) of the circuit. Additionally, the constant phase element (Q = 0.029 F) is in parallel to resistance due to the current leakage (R_{L1} = 0.003 Ω), which is in series with the Warburg diffusion element (W = 2.7 Ω/(Hz)^{½}). At low-frequency regions, the mass capacitance (C_2 = 0.025 F) is parallel to the leakage resistance (R_{L2} = 581.7 Ω). Further, the constant phase element occurs due to the non-ideal capacitor behavior, while the Warburg diffusion element shows the ion diffusion opposition. The equivalent series resistance (Rs), on the other hand, is the sum of resistances from ions' motion through the electrolyte, ions' interaction at the electrolyte/electrode interface, and the electrode/current collector interface, and the transfer resistance (R_{CT}) is due to the exchange of charges between the electrode and electrolyte ions. The C indicates the EDLC capacitance within the device. Meanwhile, R_L measures the current needed to maintain a constant voltage when the capacitor is charged and not connected to an external circuit [66]. The attained values of Rs = 5.88 Ω and R_{CT} = 2.08 Ω for the hBN/AC-1:0.05//AC in the K3_KF70 are comparable with the experimental values of Rs = 5.50 Ω and R_{CT} = 1.24 Ω, respectively, demonstrating the perfect fitting of the Nyquist plot. Likewise, the obtained small R_{CT} value of 1.24 Ω indicates low internal resistance associated with good electrical conductivity and the Faradaic reaction of the electrode in aqueous redox electrolyte. Further, resistance due to current leakage was 0.003 Ω, contributing to the deviation from the y-axis (imaginary impedance axis). At the same time, the constant phase element (Q) depresses the magnitude of the obtained semicircle, hiding its clear visibility [67]. The phase angle of the device is represented in

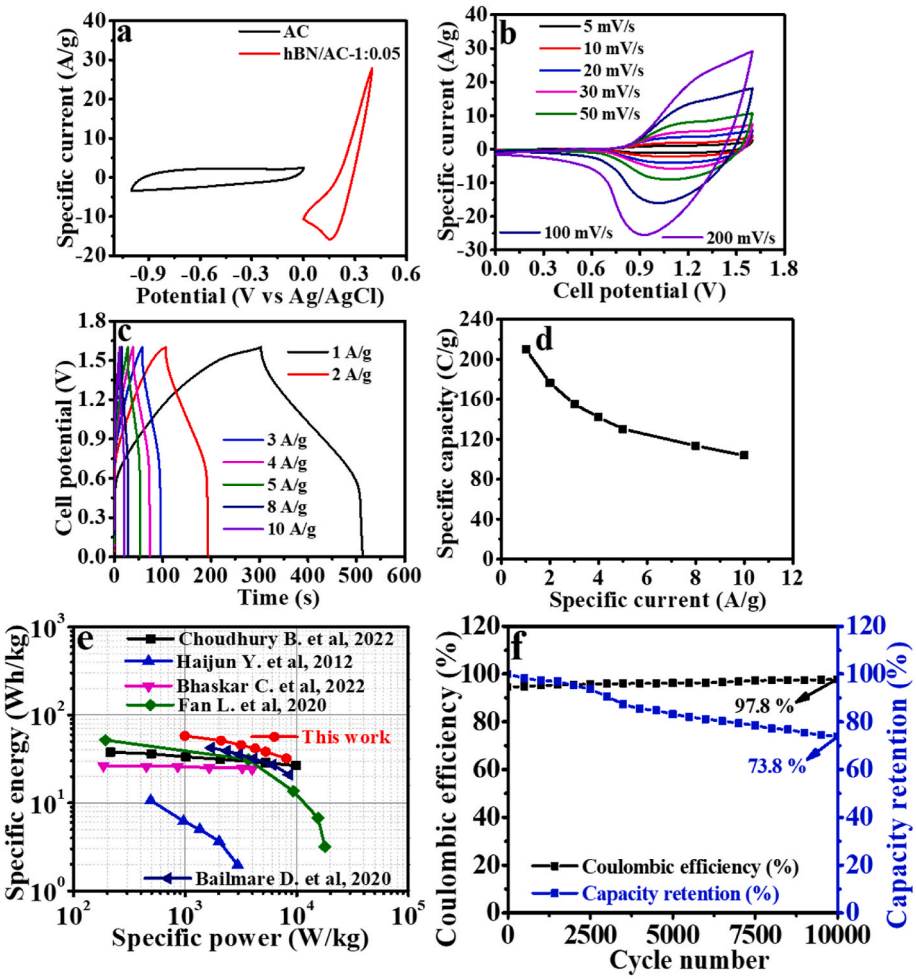

Fig. 7. (a) CV traces of the negative and positive electrode at 30 mV/s, (b) CV traces of the device at different scan rates, (c) GCD traces at a range of specific current, (d) specific capacity vs. specific current, (e) Ragone plot compared to similar devices in redox electrolytes, and (f) Coulombic efficiency and capacity retention vs. cycle number of the assembled hBN/AC-1:0.05//AC in K3_KF70.

Table 4
The electrochemical performance of redox-mediated electrolyte supercapacitors compared to the supercapacitor device developed in this study.

S/no.	Device	Redox electrolyte	Cell potential (V)	Specific energy (Wh/Kg)	Specific power (W/Kg)	Ref
1	MnO_2//MnO_2	KOH-P-Phenylenediamine (PPD)	1.0	10.12	474	[58]
2	PC-x//PC-x	$Na_2MoO_4 + Li_2SO_4$	2.0	37.24	200	[59]
3	La-COLDH//CC	2 M KOH + 0.05M $Fe(CN)_6^{3-}/Fe(CN)_6^{4-}$	1.4	42.46	1687.15	[60]
4	$W_{18}O_{49}/Ti_3C_2T_x$ Mxene //AC	1 M H_2SO_4 + 0.04 M $FeBr_3$	1.8	45.40	900	[61]
5	AC//AC	PVDF-HFP/BMIMI/CNTS	1.0	50.10	459.5	[62]
6	MBN/WS_2-3//$Ti_3C_2T_x$	PVA-KOH-KI	1.0	19.4	997.7	[63]
7	**hBN/AC - 1:0.05//AC**	**K3_KF70**	**1.60**	**58.0**	**993.7**	**This Work**

Fig. 8 (e), which shows that the device has a phase angle of −76.8°. The value is lower than −90° (for the EDLC), but close enough to this ideal value, confirming a higher contribution of the diffusion-controlled process. Fig. 8 (f) subsequently shows the real capacitance, C′(F), and imaginary capacitance, C′′(F), as a function of frequency (f). To obtain the device relaxation time, the angular frequency ($\omega = 2\pi f$) is used. The device exhibited a relaxation time ($\tau = \frac{1}{\omega}$) of 1.08 s. The displayed short relaxation time of the device is evidence that the designed supercapacitor can charge and discharge very quickly, implying that it possesses good electrical conductivity and fast ion transport between the electrode and the electrolyte, contributing to high specific energy and power [68,69].

4. Conclusion

The redox-mediated electrolyte composed of potassium ferrocyanide ($K_4Fe(CN)_6$) in potassium hydroxide (KOH) was successfully produced and reported for the first time to be used with hBN/AC-1:0.05 electrode in hybrid supercapacitors. The hBN/AC-1:0.05 electrode in the optimal electrolyte (0.07 $K_4Fe(CN)_6$ + 3 M KOH) displayed a specific capacity of 847.0C/g at 1 A/g. Further analysis of the developed device (hBN/AC-1:0.05//AC) revealed a specific capacity of 210C/g, along with corresponding specific energy and power values of 58.0 Wh/kg and 993.7 W/kg at 1 A/g, respectively. The device further established a Coulombic efficiency of 97.8 % and a matching capacity retention of 73.8 % after 10,000 GCD cycles at 5 A/g. The electrochemical analysis confirmed that the developed aqueous redox electrolyte possesses good properties,

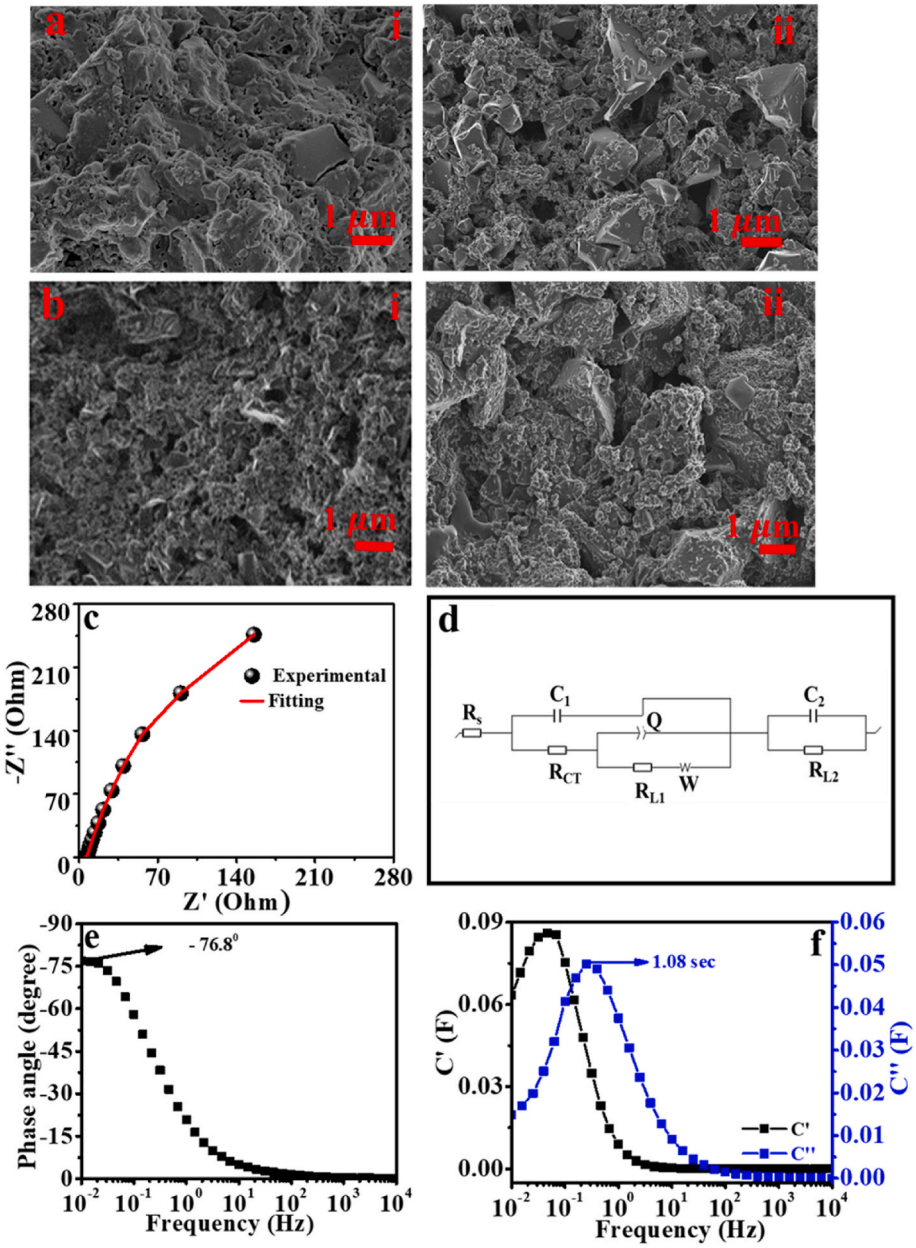

Fig. 8. SEM images of (a) positive electrode (hBN/AC-1:0.05) (i) Before cycling (ii) After stability, (b) negative electrode (AC) (i) Before cycling, (ii) After stability (c) Nyquist plot of the experimental data with the fitting curve, (d) the equivalent circuit used to fit the data in (c), (e) Bode plot, and (f) imaginary and real capacitance vs. frequency.

paving the way for its use in supercapacitors. Research findings obtained in this study demonstrate that hBN/AC composites can work effectively with redox electrolytes, leading to enhanced supercapacitor charge storage. Therefore, K3_KF70 offers potential as an aqueous redox electrolyte for supercapacitor applications.

CRediT authorship contribution statement

Hellen Ngunya Mutua: Writing – review & editing, Writing – original draft, Methodology, Investigation, Formal analysis, Data curation, Conceptualization. **Delvina Japhet Tarimo:** Writing – review & editing, Validation, Supervision, Methodology, Formal analysis, Data curation, Conceptualization. **Vusani Maphiri:** Writing – review & editing, Methodology, Formal analysis, Data curation. **Gift Rutavi:** Writing – review & editing, Methodology, Formal analysis, Data curation. **Julius Mwabora:** Writing – review & editing, Supervision, Funding acquisition. **Robinson Musembi:** Writing – review & editing, Supervision, Funding acquisition. **Ncholu Manyala:** Writing – review & editing, Validation, Supervision, Resources, Project administration, Methodology, Conceptualization.

Declaration of generative AI and AI-assisted technologies in the writing process

No AI and AI-assisted generative technologies were used in this work.

Funding

This research was supported by the DSI through NRF for the SARChI in Nano Materials for Energy storage and Water purification applications with grant number (0307208354). The opinions in this paper are those of the authors, and DSI and NRF don't take any responsibility.

Declaration of competing interest

The authors declare that they have no known competing financial interests or personal relationships that could have appeared to influence the work reported in this paper.

Acknowledgments

Hellen Ngunya Mutua gratefully acknowledges the research support provided by the Partnership for skills in Applied Sciences, Engineering, and Technology (PASET) for offering the Regional Scholarship and Innovation Fund (RSIF).

Data availability

Data will be made available on request.

References

[1] H.A. Khan, M. Tawalbeh, B. Aljawrneh, W. Abuwatfa, A. Al-Othman, H. Sadeghifar, A.G. Olabi, A comprehensive review on supercapacitors: their promise to flexibility, high temperature, materials, design, and challenges, Energy 295 (2024), https://doi.org/10.1016/j.energy.2024.131043.

[2] T. Ramachandran, S.S. Sana, K.D. Kumar, Y.A. Kumar, H.H. Hegazy, S.C. Kim, Asymmetric supercapacitors: unlocking the energy storage revolution, J. Energy Storage 73 (2023), https://doi.org/10.1016/j.est.2023.109096.

[3] M.A. Dar, S.R. Majid, M. Satgunam, C. Siva, S. Ansari, P. Arusalan, S. Rafi Ahamed, Advancements in Supercapacitor electrodes and perspectives for future energy storage technologies, Int. J. Hydrogen Energy 70 (2024) 10–28, https://doi.org/10.1016/j.ijhydene.2024.05.191.

[4] G. Qin, C. Wu, X. Song, W. He, J. Yang, X. Yu, Q. Chen, Multifunctional enhanced energy density integrated supercapacitor based on self-healing redox-mediated gel polymer electrolyte, Fuel 357 (2024), https://doi.org/10.1016/j.fuel.2023.130033.

[5] A. Meftahi, M. Shabani-Nooshabadi, A. Reisi-Vanani, Introducing GO/CuI nanostructure as active electrode matter for supercapacitors: a comparative investigation within two aqueous electrolytes, J. Energy Storage 63 (2023), https://doi.org/10.1016/j.est.2023.107077.

[6] M. Pershaanaa, S. Bashir, S. Ramesh, K. Ramesh, Every bite of Supercap: a brief review on construction and enhancement of supercapacitor, J. Energy Storage 50 (2022), https://doi.org/10.1016/j.est.2022.104599.

[7] E.P. da Silva, V.H. Fragal, E.H. Fragal, T. Sequinel, L.F. Gorup, R. Silva, E.C. Muniz, Sustainable energy and waste management: how to transform plastic waste into carbon nanostructures for electrochemical supercapacitors, Waste Manag. 171 (2023) 71–85, https://doi.org/10.1016/j.wasman.2023.08.028.

[8] D. Gao, Z. Luo, C. Liu, S. Fan, A survey of hybrid energy devices based on supercapacitors, Green Energy Environ. 8 (2023) 972–988, https://doi.org/10.1016/j.gee.2022.02.002.

[9] D.J. Tarimo, K.O. Oyedotun, A.A. Mirghni, B. Mutuma, N.F. Sylla, P. Murovhi, N. Manyala, Enhanced electrochemical performance of supercapattery derived from sulphur-reduced graphene oxide/cobalt oxide composite and activated carbon from peanut shells, Int. J. Hydrogen Energy 45 (2020) 33059–33075, https://doi.org/10.1016/j.ijhydene.2020.09.142.

[10] N.R. Nadar, R.M. Rego, G.D. Kumar, H.J. Rao, R.K. Pai, M.D. Kurkuri, Demystifying the influence of design parameters of nature-inspired materials for supercapacitors, J. Energy Storage 72 (2023), https://doi.org/10.1016/j.est.2023.108670.

[11] X. He, X. Zhang, A comprehensive review of supercapacitors: properties, electrodes, electrolytes and thermal management systems based on phase change materials, J. Energy Storage 56 (2022), https://doi.org/10.1016/j.est.2022.106023.

[12] L. Wang, J. Wu, S. Fu, A mini review of recent progress in Mo-based electrode materials for supercapacitors, Inorg. Chem. Commun. 148 (2023), https://doi.org/10.1016/j.inoche.2022.110329.

[13] C. Xiong, T. Wang, Z. Zhao, Y. Ni, Recent progress in the development of smart supercapacitors, SmartMat 4 (2023), https://doi.org/10.1002/smm2.1158.

[14] Q. Zhang, S. Xu, Y. Wang, Q. Dou, Y. Sun, X. Yan, Temperature-dependent structure and performance evolution of “water-in-salt” electrolyte for supercapacitor, Energy Storage Mater. 55 (2023) 205–213, https://doi.org/10.1016/j.ensm.2022.11.056.

[15] S. Dong, W. Gao, K. Shi, Q. Kang, Z. Xu, J. Yuan, Y. Zhu, H. Li, J. Chen, P. Jiang, G. Wu, Q. Wei, J. Qiu, X. Qian, X. Huang, Dielectric-electrolyte supercapacitors, Cell Rep. Phys. Sci. 4 (2023), https://doi.org/10.1016/j.xcrp.2023.101284.

[16] M. Wang, J. Yang, S. Liu, X. Che, S. He, G. Chen, J. Qiu, Nitrogen-doped porous carbon electrode for aqueous iodide redox supercapacitor, Chem. Eng. J. 451 (2023), https://doi.org/10.1016/j.cej.2022.138501.

[17] J. Shi, X. Tian, Y. Song, T. Yang, S. Hu, Z. Liu, Redox electrolyte-enhanced carbon-based supercapacitors: recent advances and future perspectives, Energy Mater. Device. 1 (2023) 9370009, https://doi.org/10.26599/emd.2023.9370009.

[18] B. Tiwari, A. Joshi, M. Munjal, G. Kaur, R.K. Sharma, G. Singh, Synergistic combination of N/P dual-doped activated carbon with redox-active electrolyte for high performance supercapacitors, J. Phys. Chem. Solid. 161 (2022), https://doi.org/10.1016/j.jpcs.2021.110449.

[19] G. Hariharan, S. Arunpandiyan, V. Shanmugapriya, S. Bharathi, M. Babu, B. Selvakumar, A. Arivarasan, Role of various redox additive electrolytes on the electrochemical performances of mixed metal oxide loaded multiwalled carbon nanotube based supercapacitors, J. Energy Storage 57 (2023), https://doi.org/10.1016/j.est.2022.106178.

[20] Z. Li, D. Xiao, Z. Li, Z. Xu, H. Dou, X. Zhang, Optimizing EMIMBF4-based electrolyte with LiBr redox medium for enhanced supercapacitors, J. Energy Storage 89 (2024), https://doi.org/10.1016/j.est.2024.111735.

[21] I. Ishita, P. Sahoo, P.K. Sow, R. Singhal, Unlocking the potential of KI as redox additive in supercapacitor through synergistic enhancement with H2SO4 as a co-electrolyte, Electrochim. Acta 451 (2023), https://doi.org/10.1016/j.electacta.2023.142286.

[22] M. Karnan, K. Hari Prakash, S. Badhulika, Revealing the super capacitive performance of N-doped hierarchical porous activated carbon in aqueous, ionic liquid, and redox additive electrolytes, J. Energy Storage 53 (2022), https://doi.org/10.1016/j.est.2022.105189.

[23] Y. Xiao, S. Li, C. Peng, N. Yang, S. Liu, S. Yu, Dual pseudocapacitive electrode/redox electrolyte systems for asymmetric supercabatteries, Appl. Surf. Sci. 616 (2023), https://doi.org/10.1016/j.apsusc.2023.156552.

[24] E.A. Arkhipova, R.Y. Novotortsev, A.S. Ivanov, K.I. Maslakov, S.V. Savilov, Rice husk-derived activated carbon electrode in redox-active electrolyte – new approach for enhancing supercapacitor performance, J. Energy Storage 55 (2022), https://doi.org/10.1016/j.est.2022.105699.

[25] S.A. Sawant, M.R. Waikar, G.R. Chodankar, S.R. Gurav, A.V. Patil, R.S. Vhatkar, R. G. Sonkawade, A redox additive electrolyte boosted supercapacitive energy density of wrinkled RGO sheets, J. Energy Storage 76 (2024), https://doi.org/10.1016/j.est.2023.109739.

[26] S. Sharma, P. Chand, Fabrication of ultrahigh-performance asymmetrical supercapacitor with pristine Zeolitic Imidazolate Framework-8 and a redox additive electrolyte, Mater. Sci. Semicond. Process. 158 (2023), https://doi.org/10.1016/j.mssp.2023.107383.

[27] A. Chowdhury, S. Biswas, T. Singh, A. Chandra, Redox mediator induced electrochemical reactions at the electrode-electrolyte interface: making sodium-ion supercapacitors a competitive technology, Electrochem. Sci. Adv. 2 (2022), https://doi.org/10.1002/elsa.202100030.

[28] U.V. Shembade, S.D. Dhas, M.G. Magadum, S.R. Gurav, P.G. Raje, R.G. Sonkawade, S.B. Wategaonkar, S.R. Ghatage, M.A. Gaikwad, J.H. Kim, V.G. Parale, H.H. Park, A.V. Moholkar, Investigating the effect of electrolyte and its concentration dependence on WO3 nanosheet as an efficient electrode for supercapacitors: effect of Redox Additive, J. Phys. Chem. Solid. 183 (2023), https://doi.org/10.1016/j.jpcs.2023.111609.

[29] A. Dordsheikh Torkamani, M. Velashjerdi, A. Abbas, M. Bolourchi, P. Maji, Electrodeposition of Nickel matrix composite coatings via various Boride particles: a review, J. Composite. Compound. 3 (2021) 91–98, https://doi.org/10.52547/jcc.3.2.4.

[30] C. Sharma, P. Vanishree, B. Rani, N. Lohia, G. Swati, R. Srivastava, S.N. Sharma, Electrochemical properties of two-dimensional hexagonal boron nitride nanosheets prepared by hydrothermal method, Electrochim. Acta 463 (2023), https://doi.org/10.1016/j.electacta.2023.142848.

[31] P.D.D. Singh, Z.V.P. Murthy, S. Kumar Kailasa, Metal nitrides nanostructures: properties, synthesis and conceptualization in analytical methods developments for chemical analysis and separation, and in energy storage applications, Coord. Chem. Rev. 481 (2023), https://doi.org/10.1016/j.ccr.2023.215046.

[32] H.N. Mutua, D.J. Tarimo, G. Rutavi, V. Maphiri, J. Mwabora, R. Musembi, N. Manyala, A novel study on chronoamperometry electrodeposition of hexagonal boron nitride with Eucalyptus grandis-derived activated carbon for supercapacitor applications, J. Energy Storage 107 (2025) 114968, https://doi.org/10.1016/j.est.2024.114968.

[33] G. Rutavi, D.J. Tarimo, V.M. Maphiri, V.N. Kitenge, N. Manyala, Exploration of metal-layered double hydroxide composite material for hybrid capacitor produced by facile and efficient electrodeposition process, J. Alloys Compd. 929 (2022), https://doi.org/10.1016/j.jallcom.2022.167216.

[34] D.C. Pawar, D.B. Malavekar, A.C. Lokhande, C.D. Lokhande, Facile synthesis of layered reduced graphene oxide/polyaniline (rGO/PANI) composite electrode for flexible asymmetric solid-state supercapacitor, J. Energy Storage 79 (2024), https://doi.org/10.1016/j.est.2023.110154.

[35] S.K. Soni, B. Thomas, V.R. Kar, A comprehensive review on CNTs and CNT-Reinforced composites: syntheses, characteristics and applications, Mater. Today Commun. 25 (2020), https://doi.org/10.1016/j.mtcomm.2020.101546.

[36] M.B. Toffolo, I. Pinkas, A.Á. Gallo, E. Boaretto, Crystallinity assessment of anthropogenic calcites using Raman micro-spectroscopy, Sci. Rep. 13 (2023), https://doi.org/10.1038/s41598-023-39842-8.

[37] S. Ali, P.M. Ismail, M. Humayun, M. Bououdina, Hexagonal boron nitride: from fundamentals to applications, Desalination 599 (2025), https://doi.org/10.1016/j.desal.2024.118442.

[38] T. Li, X. Jiao, T. You, F. Dai, P. Zhang, F. Yu, L. Hu, L. Ding, L. Zhang, Z. Wen, Y. Wu, Hexagonal boron nitride nanosheet/carbon nanocomposite as a high-performance cathode material towards aqueous asymmetric supercapacitors, Ceram. Int. 45 (2019) 4283–4289, https://doi.org/10.1016/j.ceramint.2018.11.101.

[39] J. Yang, X. Hu, X. Fang, L. Fan, G. Qin, Z. Zhang, J. Xu, Y. Liang, Q. Chen, Tough and redox-mediated alkaline gel polymer electrolyte membrane for flexible supercapacitor with high energy density and low temperature resistance, J. Membr. Sci. 650 (2022), https://doi.org/10.1016/j.memsci.2022.120386.

[40] A.S. Samsudin, N.M. Ghazali, N.F. Mazuki, K. Aoki, Y. Nagao, The ionic conductivity and electrochemical performance of Alginate-PVA based polymer electrolyte with Li+ charge carriers for supercapacitor, J. Electroanal. Chem. 967 (2024), https://doi.org/10.1016/j.jelechem.2024.118463.
[41] V.N. Kitenge, D.J. Tarimo, K.O. Oyedotun, G. Rutavi, D.T. Bakhoum, N. Manyala, Electrical double-layer capacitor based on low aqueous electrolyte contents in EmimTFO ionic liquid, Int. J. Energy Res. 2023 (2023), https://doi.org/10.1155/2023/8659009.
[42] A.H. Anwer, M.M. Zubair, F. Mashkoor, A. Benamor, I. Hasan, M. Shoeb, C. Jeong, Enhancing the electrochemical performance of hybrid supercapacitors with in-situ grown ultrasound-mediated heterostructure bi-metallic and dual-linker MOF nanoarchitecture by harnessing charge storage mechanisms, J. Alloys Compd. 970 (2024), https://doi.org/10.1016/j.jallcom.2023.172512.
[43] B. Chettiannan, E. Dhandapani, G. Arumugam, R. Rajendran, M. Selvaraj, Metal-organic frameworks: a comprehensive review on common approaches to enhance the energy storage capacity in supercapacitor, Coord. Chem. Rev. 518 (2024), https://doi.org/10.1016/j.ccr.2024.216048.
[44] H. Yu, J. Liu, X. Wu, R. Li, R. Jin, G. Zhou, Construction of mesocrystal Cu2-xSe nanoplates with high infiltration for enhanced electrochemical performance in lithium ion batteries and electrochemical supercapacitors, Appl. Surf. Sci. 655 (2024), https://doi.org/10.1016/j.apsusc.2024.159530.
[45] S. Shegokar, L. Bharti, S. Anshu, S. Priya, A.K. Srivastava, A. Chandra, Modulating interfacial interactions by using redox additives alongwith carbon decorated ZIF-67 electrodes for efficient Al-ion based battery supercapacitor hybrids, Electrochim. Acta 514 (2025), https://doi.org/10.1016/j.electacta.2024.145611.
[46] A.A. Moya, Low-frequency approximations to the finite-length Warburg diffusion impedance: the reflexive case, J. Energy Storage 97 (2024), https://doi.org/10.1016/j.est.2024.112911.
[47] C. Peng, X. Huang, M. Zhao, S. Li, S. Liao, S. Yu, Redox-active hydrogel electrolytes for carbon-based flexible supercapacitors over a wide temperature range, Carbon N Y 229 (2024), https://doi.org/10.1016/j.carbon.2024.119497.
[48] A. Surulinathan, H. Gubendran, B. Sambandam, S. Ganapathy, A. Ayyaswamy, Mixed metal oxide-based binder-free electrode and redox additive electrolyte combination for enhanced supercapacitor performance, J. Alloys Compd. 988 (2024), https://doi.org/10.1016/j.jallcom.2024.174164.
[49] X. Tian, T. Yang, Y. Song, Y. Li, H. Peng, R. Xue, X. Ren, Z. Liu, Symmetric supercapacitor operating at 1.5 V with combination of nanosheet-based NiMoO4 microspheres and redox additive electrolyte, J. Energy Storage 47 (2022), https://doi.org/10.1016/j.est.2022.103960.
[50] A. Mamani, D. Barreda, M. Fabiana Sardella, M. Bavio, C. Blanco, Z. González, R. Santamaría, Fe-doped biomass-derived activated carbons as sustainable electrode materials in supercapacitors using different electrolytes, J. Electroanal. Chem. 965 (2024), https://doi.org/10.1016/j.jelechem.2024.118366.
[51] G. Rutavi, D.J. Tarimo, V.M. Maphiri, V.N. Kitenge, K.O. Otun, H.N. Mutua, N. Manyala, Evaluation of manganese chromium metal organic framework and cobalt nickel iron layered double hydroxide composite synthesised by electrodeposition for supercapacitor applications, J. Alloys Compd. 1037 (2025), https://doi.org/10.1016/j.jallcom.2025.182271.
[52] Y. Luo, S. Wang, Y. Xu, N. Liu, L. Dong, Y. Shen, F.G. Zhao, Exploring redox-active electrolytes to boost energy density of carbon-based supercapacitors, J. Colloid Interface Sci. 684 (2025) 729–734, https://doi.org/10.1016/j.jcis.2025.01.082.
[53] B.J. Choudhury, K. Ingtipi, V.S. Moholkar, Improved energy density of reduced graphene oxide based aqueous symmetric supercapacitors in redox-active and "water-in-salt" electrolytes, J. Energy Storage 52 (2022), https://doi.org/10.1016/j.est.2022.105006.
[54] P. Haldar, Use of redox additive to enhance the electrochemical performance of Co3O4/polyaniline/graphene composite-based supercapacitors, J. Mater. Sci. Mater. Electron. 31 (2020) 7905–7915, https://doi.org/10.1007/s10854-020-03329-3.
[55] S.A. Kumar, V. Thirumal, N.H. Alotaibi, S. Mohammad, J. Kim, V. Siva, K. Selvakumar, A. Murugan, Synthesis and characterization of SnO2-La2O3 for electrochemical supercapacitor performance in redox additive electrolyte, Ionics 30 (2024) 4163–4177, https://doi.org/10.1007/s11581-024-05528-y.
[56] B. Ramulu, J.A. Shaik, A.R. Mule, J.S. Yu, Improved rate capability and energy density of high-mass hybrid supercapacitor realized through long-term cycling stability testing and selective electrode design, Mater. Sci. Eng. R Rep. 160 (2024), https://doi.org/10.1016/j.mser.2024.100820.
[57] S. Chen, X. Zhou, X. Ma, L. Li, P. Sun, M. Zhang, Asymmetric supercapacitors with excellent rate performance by integrating Co(OH)F nanorods and layered Ti3C2T: x paper, RSC Adv. 9 (2019) 30957–30963, https://doi.org/10.1039/c9ra06393e.
[58] H.J. Yu, J.H. Wu, L.Q. Fan, Y.Z. Lin, S.H. Chen, Y. Chen, J.L. Wang, M.L. Huang, J. M. Lin, Z. Lan, Y.F. Huang, Application of a novel redox-active electrolyte in MnO 2-based supercapacitors, Sci. China Chem. 55 (2012) 1319–1324, https://doi.org/10.1007/s11426-012-4673-z.
[59] B.J. Choudhury, H.H. Muigai, P. Kalita, V.S. Moholkar, Biomass blend derived porous carbon for aqueous supercapacitors with commercial-level mass loadings and enhanced energy density in redox-active electrolyte, Appl. Surf. Sci. 601 (2022), https://doi.org/10.1016/j.apsusc.2022.154202.
[60] D.B. Bailmare, P. Tripathi, A.D. Deshmukh, B.K. Gupta, Designing of two dimensional lanthanum cobalt hydroxide engineered high performance supercapacitor for longer stability under redox active electrolyte, Sci. Rep. 12 (2022), https://doi.org/10.1038/s41598-022-06839-8.
[61] S. Liu, T. Zeng, Y. Zhang, Q. Wan, N. Yang, Coupling W18O49/Ti3C2Tx MXene pseudocapacitive electrodes with redox electrolytes to construct high-performance asymmetric supercapacitors, Small 18 (2022), https://doi.org/10.1002/smll.202204829.
[62] L.Q. Fan, Q.M. Tu, C.L. Geng, Y.L. Wang, S.J. Sun, Y.F. Huang, J.H. Wu, Improved redox-active ionic liquid-based ionogel electrolyte by introducing carbon nanotubes for application in all-solid-state supercapacitors, Int. J. Hydrogen Energy 45 (2020) 17131–17139, https://doi.org/10.1016/j.ijhydene.2020.04.193.
[63] S. De, S. Acharya, C.K. Maity, G.C. Nayak, Boron Nitride/Ti3C2Tx MXene Nanosheet/WS2 nanostructure ternary composites for all-solid-state flexible asymmetric supercapacitors, ACS Appl. Nano Mater. 6 (2023) 11175–11186, https://doi.org/10.1021/acsanm.3c01202.
[64] T. Schoetz, L.W. Gordon, S. Ivanov, A. Bund, D. Mandler, R.J. Messinger, Disentangling faradaic, pseudocapacitive, and capacitive charge storage: a tutorial for the characterization of batteries, supercapacitors, and hybrid systems, Electrochim. Acta 412 (2022), https://doi.org/10.1016/j.electacta.2022.140072.
[65] P. Bhojane, Recent advances and fundamentals of Pseudocapacitors: materials, mechanism, and its understanding, J. Energy Storage 45 (2022), https://doi.org/10.1016/j.est.2021.103654.
[66] T. Meng, B. Ramasubramanian, S. Sundarrajan, Y. Xuan, S. Ramakrishna, Unleashing capabilities of supercapacitors: strategies to reduce internal resistances, J. Power Sources 596 (2024), https://doi.org/10.1016/j.jpowsour.2024.234068.
[67] D. Hilmi, S. Zaim, A. Mortadi, I. Sabir, M. Monkade, R. Nmila, A.V. Ursu, C. Vial, P. Michaud, H. Rchid, R. El Moznine, Complex conductivity as a tool to investigate the electrical behavior between graphene oxide and reduced graphene in supercapacitors: correlation between the electrical properties, Results Eng. 23 (2024), https://doi.org/10.1016/j.rineng.2024.102673.
[68] S. Li, Z. Li, D. Xu, G. Feng, R. Hu, Porosity and tortuosity: keys for accurate modeling of porous electrodes in supercapacitors, Mater. Today Phys. 36 (2023), https://doi.org/10.1016/j.mtphys.2023.101174.
[69] S. Zhu, Y. Chang, W. Hou, Y. Li, J. Ni, G. Han, Molten-salt directed mesopore engineering of carbon nanotubes for energetic quasi-solid-state supercapacitors, Carbon N Y 200 (2022) 75–83, https://doi.org/10.1016/j.carbon.2022.08.030.